Probing the internal structure of nuclepore with hysteretic capillary condensation

M. P. Lilly* and R. B. Hallock†
Laboratory for Low Temperature Physics, Department of Physics, University of Massachusetts, Amherst, Massachusetts 01003
(Received 25 August 2000; published 30 March 2001)

We report filling (adsorption) and draining (desorption) measurements of superfluid ^{4}He in the porous material nuclepore. These low-temperature measurements explore the classical hysteretic properties of the capillary condensation of the liquid, while utilizing the propagation of third sound in the superfluid helium as an *in situ* probe of the chemical potential. We present measurements of global hysteresis loops, subloops, and reversal curves. With this data, we determine that the interconnected pore structure of the material is critical to the draining process. In addition, we present measurements of the connectivity and pore size distributions for nuclepore, and compare these results to calculations and earlier measurements. This work establishes the utility of the novel working fluid superfluid ^{4}He and the applicability of the techniques used here for such studies of porous materials.

DOI: 10.1103/PhysRevB.63.174503 PACS number(s): 67.40.Rp, 67.40.Hf, 67.40.Pm

I. INTRODUCTION

The presence of curved surfaces in many materials has important consequences for the adsorption of liquids. Due to surface tension, adsorbed films have a thickness that depends on surface curvature, and if the material has open voids, or pores, the liquid-vapor surface tension can cause capillary condensation, which occurs when the surface tension makes the presence of bulk liquid in the pores more favorable than a film coating on the pore surfaces. This process is usually hysteretic and depends strongly on the size of the pores and the nature of the pore network. This sensitivity to the details of the interior of the porous material allows a nondestructive technique for determining the pore sizes and connectivity using hysteresis data.

Early models of hysteretic capillary condensation treated the pore space simply as a large group of independent pores.[1] Each pore was regarded as a tiny two-state system; either the pore was filled or empty. The pores could switch between these states in response to changes in the chemical potential of the system. This independent-pore model of hysteresis, the Preisach model,[2] originated in studies of the hysteresis shown by magnetic systems. Methods to use measurements of the global hysteresis are available and can be used to estimate pore sizes. Such simple models neglect one of the main features of most porous systems: internal pores.[3] In an effect called pore blocking, an internal pore (i.e., one with no access to the surface vapor) cannot drain until at least one of its neighbors has drained, regardless of its size. In fact, hysteresis can arise from pore blocking alone (without the individual pores being hysteretic). For systems where pore blocking dominates the hysteresis, Mason[4,5] has developed a general recipe for using experimental data to find both the pore size distribution (PSD) and the connectivity of the pores. Although the assumptions of the Mason model are not ideally suited to a material such as nuclepore, we will find it productive to apply the model to our data.

In this paper, we report measurements of the hysteretic capillary condensation[6–10] of superfluid ^{4}He in the porous material nuclepore[11] and observe, among other things, return point memory,[6] a lack of congruence between subloops with the same chemical-potential endpoints,[6,8] and avalanches[6,10] among the draining pores during withdrawal of the ^{4}He. Nuclepore is a commercially fabricated porous thin polycarbonate membrane material with nearly cylindrical pores completely penetrating the membrane. Ideally, pore blocking would not be important. The primary filling and draining curves[12] are determined by measurements in which the amount of fluid present in the nuclepore is measured as a function of chemical potential for filling and draining. Interestingly, when all of the pores are filled, slight changes in the liquid density as a function of chemical potential are observed and can be attributed to the compressibility of liquid helium. Using chemical potential trajectories that create subloops in the hysteretic region, we observe closed subloops that exhibit return point memory (RPM), a phenomenon in which reversals of the direction of changes in the chemical potential return the system to a previous configuration. The Preisach model correctly explains this feature, yet fails to account for differences in the shape of hysteretic subloops that span identical chemical potential endpoints. This failure of shape congruence indicates that interactions between pores are important, perhaps due to pore-pore intersections within the material. A modified version of the Preisach model is developed that includes a weak interaction between pores of a pore-blocking nature. While this modification can qualitatively account for features such as subloop shapes, quantitative determination of the pore sizes and connectivity is not possible. Since pore blocking does appear to occur in nuclepore, the analysis approach of Mason is used and results for the PSD and pore connectivity are presented.

In Sec. II nuclepore is described in more detail. Also described are the properties of capillary condensation in a cylindrical pore and the Preisach model. In Sec. III, the experimental techniques we have used for measuring hysteresis curves are described. The data and interpretations are presented in Sec. IV.

II. CAPILLARY CONDENSATION AND HYSTERESIS

Capillary condensation is an inherently hysteretic process. A single pore of a given shape and size will fill and drain at

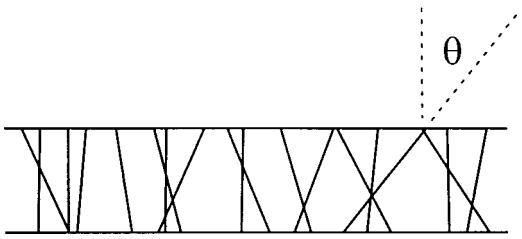

FIG. 1. Cross section of nuclepore (not to scale). Cylindrical pores penetrate the material up to an angle $\theta_{max} \approx 34°$ from the normal. The length-to-diameter ratio for the pores is 50.

different values of the chemical potential. While generally complicated, the filling and draining characteristics of simple shapes, such as cylinders, can be determined analytically. The hysteresis generated by the filling and draining of the voids in a porous material can be modeled using two quite different approaches. In the first, the Preisach model, the inherent hysteresis present for a single pore is the origin of the observed hysteresis, and in this model all pores fill and drain *independently*. In the second, a model attributed to Mason, when pore blocking is important, hysteresis arises due to the *interconnections* among voids in the pore network.

A. Nuclepore

Our choice of porous material for these experiments plays an important role in the interpretation and design of the experiments. Initially, nuclepore was chosen for its expected relative simplicity. It is a commercially designed and fabricated material whose primary use is a filter material in biological applications. Nuclepore is composed of nearly cylindrical pores that pass completely through the material and nuclepore is not expected to have internal pores that fail to connect to the surface of the material. However, the cylinders do intersect one another due to the high pore density. To produce nuclepore a thin polycarbonate membrane is drawn across a radioactive source with a poorly collimated flux. The radiation creates damage tracks in the plastic material, and these damaged regions are preferentially etched away with a chemical process. The resulting pores are nearly cylindrical with a narrow spectrum of radii. Due to the collimation, the axis of the pores is tilted at an angle θ from normal, $0 \leqslant \theta \leqslant 34°$ as sketched in Fig. 1, and the in-plane projection angle ϕ is random, $0 \leqslant \phi < 360°$. The material is available in a range of pore sizes. It should be noted that the pores are not perfectly cylindrical; they have a slightly barrel shape. This was determined by flowing different fluids through the membranes,[13] and this interpretation is consistent with the capillary condensation results of Smith, Godshalk and Hallock.[14] In this work we study material[15] with nominal pore diameters of 200 and 30 nm.

A number of previous studies of nuclepore exist. Valles, Smith and Hallock[16] made pulsed third-sound measurements for superfluid ^{4}He on nuclepore with 200-nm-diameter pores and found that the index of refraction was hysteretic due to the capillary condensation of the pores. Smith, Godshalk, and Hallock[14] made simultaneous capacitive and third-sound measurements on nuclepore with 80- and 200-nm-diameter pores. They studied the onset of superfluidity and determined the pore size distribution from both the hysteretic capillary condensation and third-sound data assuming that the pores do not interact. Godshalk and Hallock[17] expanded these studies to include 30- and 100-nm-diameter nuclepore and performed a Brunauer-Emmett-Teller (B.E.T.) analysis on the low coverage adsorption data.

Since the material consists of long thin cylindrical-shaped pores with well-defined orientations, it seems to be a simple-pore network where the assumption that the pores act independently might be justified. Pore size distribution calculations attributed to Smith *et al.*[14] were carried out presuming independently acting pores having two characteristic radii, one for filling and one for draining. Lilly *et al.*[6] found that for a range of chemical-potential values the draining process in nuclepore occurs in discrete steps, or avalanches. Without discrete ''clumping'' of pores at a set of specific sizes (not likely, considering the manufacturing process), the presence of avalanches indicates that the behavior of one pore can affect the behavior of other pores in the system; i.e., the pores must interact with one another. This conclusion has motivated our more-detailed studies of the hysteresis behavior of ^{4}He in nuclepore.

One possible interaction mechanism is pore blocking. The relevance of pore blocking in nuclepore depends on how well connected the pores are inside the material. With a simple computer simulation that uses the nominal parameters for the pore density n, the cylinder radius R, and the membrane thickness t, we calculate the number of other pores that intersect at a given pore. To do this, an array of 2000 ''pores'' is created, where the ith pore is randomly assigned a base position $(x_i, y_i, z_i = 0)$ and angles (θ_i, ϕ_i) for pore inclinations. From these parameters, each pore is assigned a vector $\vec{v}_i$ aligned along the pore axis. For any two pores i and j, the closest approach of the axes is

$$d = \frac{|\vec{u}_{ij} \cdot \vec{v}_i \times \vec{v}_j|}{|\vec{v}_i \times \vec{v}_j|}, \tag{1}$$

where $\vec{u}_{ij}$ is the vector between the base positions (x_i, y_i) and (x_j, y_j). If $d < 2R$ and the axes are closer than $2R$ within the membrane $(0 < z < t)$, then pores i and j intersect. Finite-size effects at the edges of the system lead to an undercounting of the number of intersections. Histograms of the number of pores with 0, 1, etc. intersections for 30-, 80-, and 200-nm-diameter nuclepore are shown in Figs. 2(a), (b), and (c). For 200-nm nuclepore, the mean is 5.3 intersections for each pore, with a wide spread (from 0–15 intersections). Keeping the thickness and the density fixed while decreasing the pore radius decreases the average number of intersections a given pore experiences.

Also important is the net interconnection among the pores throughout the system. A second simulation tested for percolation. A material is percolated when it is possible to cross from one side to the other entirely by connected pores within the material. In this simulation, 100 realizations of a pore system are created for pores from 5–100 nm in diameter. These systems of pore networks range from 100–1000 pores

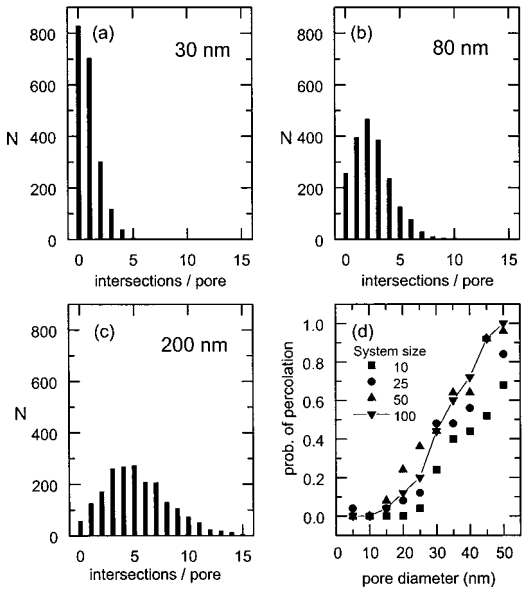

FIG. 2. Nuclepore simulation results for the number of intersections per pore and the probability of percolation. Histograms of the number of intersections per pore are shown for (a) 30-nm, (b) 80-nm, and (c) 200-nm pore-diameter nuclepore. In (d) the percolation probability for several simulation sizes is shown.

(in an effort to identify the presence of finite-size effects). In each such network the largest cluster of connected pores is identified and if this cluster spans the system then that particular realization is defined to be percolated. The probability of percolation is the number of percolated realizations divided by the number of realizations. The results for this percolation probability study are shown in Fig. 2(d). The pores in 200-nm nuclepore are completely percolated. Reduction of the pore diameter to 30 nm leads to only a $\sim 50\%$ probability of percolation. These results are consistent with those obtained by Guyer and McCall[18] where, using mean-field arguments, they find that the percolation threshold is reached for 40–50-nm-diameter pores.

B. Adsorption and capillary condensation

A surface exposed to the vapor of an adsorbate will develop a liquid film on the surface provided that the adsorbate wets the material.[19] The van der Waals attraction between the surface and vapor allows this liquid film to coexist with the gaseous phase, even for pressure P far below saturated vapor pressure P_0. In equilibrium, the film thickness is determined by equating the chemical potentials of the film μ_f and the gas phase μ_g.[20] In this paper, the chemical potential μ will be expressed relative to the chemical potential at the surface of the bulk liquid phase μ_0 (i.e., we adopt the convention that $\mu_0=0$). For the vapor,

$$\mu_g = T\ln(P/P_0). \tag{2}$$

The van der Waals potential for a film on a flat surface is given by

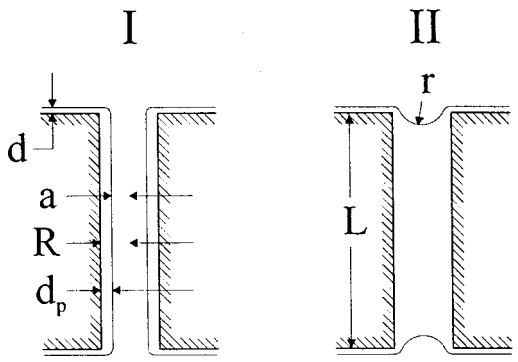

FIG. 3. Cross section of a cylindrical pore (not to scale). When empty (I), a liquid film forms on the surfaces. On a flat surface, the film thickness is d. Inside the pore, the thickness is d_p, $d_p>d$. When full (II), a meniscus with radius r is present at the pore openings. L is the thickness of the nuclepore.

$$\mu_{vdW,flat} = -\frac{\gamma\xi}{d^3(d+\xi)}. \tag{3}$$

Here d is the film thickness, γ is the strength of the attraction between the substrate and the adsorbing vapor,[21] and ξ is a relativistic correction[22,23] important for thick films. For thin films ($d \ll \xi$) we can use $\mu_{vdW} \approx -\gamma/d^3$. The chemical potential of a film on a curved surface will include both the van der Waals potential due to the substrate and an additional term for the surface tension σ of the liquid-vapor interface

$$\mu_f = \mu_{vdW} - \frac{\sigma V_m}{r_K}, \tag{4}$$

where V_m is the molar volume and r_K the mean curvature of the interface.

As we have noted, the pores of nuclepore are nominally expected to be cylindrical. Capillary condensation has been considered in detail for cylindrical pores by Saam and Cole,[24,25] and these calculations will provide the basis for the basic hysteresis element for the Preisach model discussed in the next section. Consider a cylindrical pore with length L and radius R, sketched in cross section in Fig. 3. At low chemical potentials [Fig. 3(a)], the film thickness on the pore walls d_p is larger than on the flat surfaces d. Using the definitions $a=R-d_p$ and $y=a/R$, Saam and Cole find the form of the chemical potential in the pore μ_p to be

$$\mu_p = U(a) - \sigma V_m/a;$$

$$U(a) = -\frac{3\pi\gamma}{2R^3} F\left(\frac{3}{2},\frac{5}{2};1,y^2\right), \tag{5}$$

where $U(a)$ is the van der Waals potential for a cylinder and F is the hypergeometric function. For $y\sim 1$, the van der Waals potential becomes approximately that of a thin flat film $U(a)\sim -\gamma/d^3$. Further increasing μ leads to an instability in d_p, and a sudden transition from configuration I to

II (Fig. 3) occurs at a chemical potential that we label μ_α. The chemical potential for the filling instability is found using

$$\frac{R^2}{R_0^2}=\frac{15}{4}y_c^2(1-y_c)P_{3/2}^1\left[\frac{1+y_c^2}{1-y_c^2}\right], \tag{6}$$

where $R_0=\sqrt{3\pi\gamma/\sigma V_m}$ is a scaling parameter and $P_{3/2}^1(x)$ is the associated Legendre function. Numerically solving Eq. (6) for the film thickness y_c and then using Eq. (5) leads to the chemical potential for filling μ_α. After the pore is filled, a meniscus with radius r forms at the ends of the cylinder, where

$$\mu=-\frac{2\sigma V_m}{r}, \tag{7}$$

with the mean radius of curvature $r_K=2/r$. Upon decreasing the chemical potential, r decreases and eventually the fluid in the pore is unstable to draining. For large pores (such as the pores in this study), the pore will drain at the chemical potential μ_β when $r\approx R$

$$\mu_\beta=-\frac{2\sigma V_m}{R}. \tag{8}$$

As an example, we calculate the chemical potentials for filling (μ_α) and draining (μ_β) using the parameters for 200-nm-diameter nuclepore. At $T=1.52$ K, using Eq. (6) we find $R/R_0=22.14$ and numeric inversion results in $y_\alpha=0.842$ ($d_p\approx 44$ layers, 1 layer = 0.36 nm). The chemical potential for filling is determined using Eq. (5) and is $\mu_\alpha=-0.0135$ K. Draining occurs when $r\approx 200$ nm, and using Eq. (8), $\mu_\beta=-0.0216$ K ($d_p\approx 17$ layers, $d\approx 13$ layers).

C. Independent pores

In a system where a collection of noninteracting two-state hysteretic elements produces global hysteresis, the Preisach model provides a general framework for modeling the hysteresis. This model originated in studies of magnetic materials by Preisach[2] in 1935. The two-state element in magnetic systems is a single magnetic domain whose magnetization will be aligned or opposed to an external magnetic field, depending on the field strength and history. A bulk magnetic material is made up of many domains, and the Preisach model allows predictions of hysteresis curves based on knowledge of the individual elements. Since its original incarnation in magnetic systems, the Preisach model has been adapted to other hysteretic systems such as stress-strain hysteresis in martensitic materials[26] and rocks,[27] and capillary condensation in porous materials.[1,28] More important than simply predicting hysteresis curves, techniques have been developed to invert the process. Mathematical tools for taking experimental hysteresis data from the global system and extracting information about the microscopic elements have been developed by Mayergoyz and Doong[29,30] and McCall and Guyer.[31] If a capillary condensation system were composed of noninteracting hysteretic elements, these tools would allow a nondestructive way to estimate the pore size distribution.

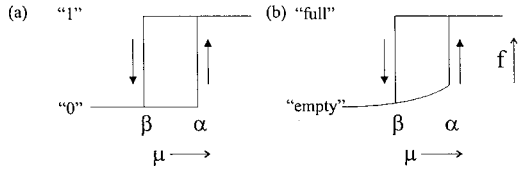

FIG. 4. Hysteresis of the independent hysteretic element in the Preisach model. In (a), the most basic hysteresis loop is shown. The $f=0\rightarrow 1$ transition occurs at $\mu=\alpha$, and the $f=1\rightarrow 0$ transition occurs at $\mu=\beta$. In (b), the ''unfilled pore'' is allowed to have a film form on the surface, and the empty state is no longer $f=0$, but becomes $f=f(\mu)$.

An example of the basic hysteretic behavior of a single element (a pore in our case) is shown in Fig. 4(a). Upon increasing an external potential μ, the system switches from ''0'' to ''1'' at the point labeled α. When decreasing μ, a second switching point occurs when the state changes from ''1'' to ''0'' at β. This general picture is adapted to capillary condensation in Fig. 4(b). Now, the two states are ''empty'' and ''full.'' The external potential is the chemical potential. When empty, a film is present on the surface of the pore and the growth of film thickness with an increase in chemical potential gives rise to a growth in the amount of fluid in the porous material before any capillary condensation occurs. Identifying f as the percentage that a pore is filled (the filling fraction or filling factor), there is a (nonhysteretic) increase of f in the ''empty'' state with an increase in μ due to the presence of the film. Note that $\alpha\geqslant\beta$ since a pore must be empty before it can fill. In the calculated example of the 200-nm cylinder given above, $\alpha=-0.0135$ and $\beta=-0.0216$ K.

To illustrate how hysteresis curves can be calculated, we will simulate a collection of noninteracting ''pores'' using a random distribution of N pores, either full (weight $1/N$) or empty (weight 0). The film on the surface of the ''empty'' pores is neglected in this example. Each of the pores is characterized by a pair of chemical-potential values for filling and draining, labeled (α_i,β_i) for the ith pore. A mapping onto the α-β plane will represent each pore in the system of nonidentical pores by a unique point. Since the pore must fill before it drains, $\alpha_i\geqslant\beta_i$, all pores in the system are mapped onto a triangular region indicated in Fig. 5(a). Each pore in the specific porous system is represented by a single small circle in Fig. 5(a). In Figs. 5(c) and (e), the hatched regions represent the pores that are filled and we will discuss these shortly. For clarity, the collection of pores is only shown in detail by small open circles in Fig. 5(a), but this distribution of small circles should be presumed to be present in each of the Figs. 5(a), (c), (e), and (g). The right column in Fig. 5 contains panels that show the evolving hysteresis loop at various stages of the evolution of the chemical potential. In the right set of panels the bottom axis is the external potential and the left axis is the normalized filling fraction, where $f=1$ when all of the pores are filled. The rule for keeping track of which pores are filled and which are empty is this:

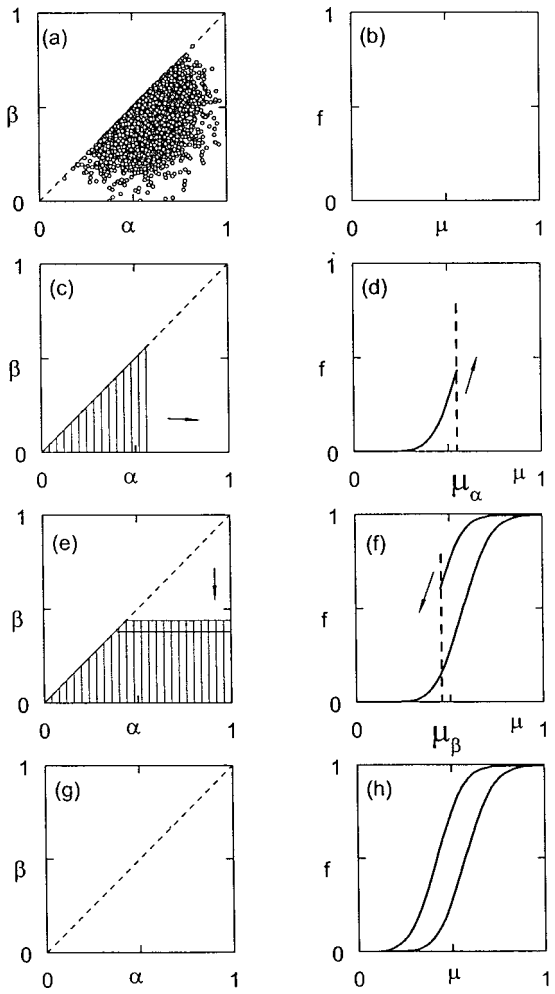

FIG. 5. Example to illustrate using the Preisach model. In (a), a collection of elements (pores in our case) can be mapped onto α-β space, each element represented by a single point. The shaded regions in (c) and (e) indicate what set of pores (α_i,β_i) are capillary condensed as the chemical potential is increased and then decreased. In (d), (f), and (h) the corresponding evolution of the hysteresis loop is traced out. μ_α and μ_β are the values of the chemical potential at the specific example points in the evolution of the hysteresis curve.

increasing the chemical potential by a small amount from μ_0 to $\mu_0+d\mu$ causes all pores with α values between μ_0 and $\mu_0+d\mu$ [represented by one of the vertical strips in Fig. 5(c)] to fill (unless they are already filled, of course). Decreasing the chemical potential by $d\mu$ causes all pores with β values between μ and $\mu-d\mu$ [represented by a single representative horizontal strip in Fig. 5(e)] to drain (unless they are already empty). The global hysteresis loop is created by first increasing μ and filling all of the pores, a process underway in Figs. 5(c) and (d). Then, once the pores have been filled, the chemical potential is decreased and pores drain as shown in Figs. 5(e) and (f). In Figs. 5(g) and (h), the process is shown as complete (all the pores are empty) and the global hysteresis loop that has been traced out by the system is shown. With a different initial distribution of (α_i,β_i), i.e., a different distribution of pore sizes, this global loop would have a different shape. More complicated

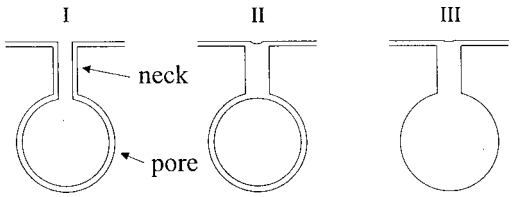

FIG. 6. Internal pores exhibit pore blocking. As the chemical potential is increased, the pore and the neck will start empty, with only a thin film growing on the walls (I). The neck will capillary condense first (II) and then the pore (III). Upon draining, the pore would drain before the neck to reach (II), but unless a bubble nucleates in the pore, this situation is impossible. The pore will go from III→I during draining.

chemical-potential changes can be used (e.g., lowering μ before it has reached its maximum value) to create subloops within the global loop.

D. Interconnected pores

Determining the pore size distribution (PSD) of an arbitrary porous material is one of the motivating goals of those studying hysteresis due to capillary condensation. If the Preisach model correctly predicted the hysteresis behavior for capillary condensation, then it could easily be used to calculate the PSD [i.e., the distribution (α_i,β_i)] by using the measured hysteresis loop and the relations between surface tension, pore size, and capillary condensation. Unfortunately, this simple model leaves out any detail about how the pores are connected in the interior of the porous material. As a result of connectivity, *pore blocking* can occur. The Preisach model is unable to account for this effect, and in spite of its utility in motivating an understanding of features of hysteresis loops, the Preisach model is generally not very useful for determining PSD's from experimental hysteresis loop data.

Pore blocking occurs when a large internal pore can access the external vapor only via smaller connecting pores. This is shown schematically for an ordinary fluid for an extreme example in Fig. 6 where in (I), a large internal pore is connected by a narrow neck to the outside of the porous material. When the chemical potential is increased, the narrow neck will fill first (II). Even though the neck is filled with liquid, the film in the pore continues to thicken as if the neck were not there. Eventually the large pore will capillary condense (III). Now, if the pore starts filled with liquid (III) and the chemical potential is decreased, eventually (II) would be possible, but only if a bubble is nucleated in the pore (not likely for pores larger than a few nanometers in diameter[1]). In this case, only after the neck drains will the large pore be able to drain; the large pore must have *access* to the external vapor in the cell. This effect only affects the desorption process; on adsorption, the interior pores (with ''bubbles'' already present) are still in contact with the outside chemical potential and fill normally. The presence of pore blocking can have an influence on the dynamics of hysteretic capillary condensation. For example, for the case of a very viscous fluid with low vapor pressure, interior open pores such as that represented by Fig. 6 (II) can have delayed

reactions to changes in the external chemical potential. We have chosen superfluid ^{4}He as our working fluid to reduce this effect.

In an effort to address the problem of pore blocking, a number of models that include pore-pore interconnections have been developed. Using Monte Carlo methods on a three-dimensional lattice of voids and necks, Wall and Brown[32] calculated results that fit some experimentally observed hysteresis curves better than did the independent pore model. Mason[4,5] used similar ideas, but included a method to allow the PSD and also the pore connectivity to be determined using experimental data from measurements of the secondary draining. Interestingly, the hysteresis in Mason's model arises *entirely* from pore blocking; the individual elements are not hysteretic. Although it is clearly an oversimplification to completely neglect single pore hysteresis for a material such as nuclepore, which has predominantly cylindrical pores, we will apply Mason's model in an effort to extract quantitative results of pore size distributions and connectivity in the last section of this paper.

III. EXPERIMENTAL DESIGN

We set out to make detailed measurements of the filling and draining behavior that is due to capillary condensation for ^{4}He in the porous material nuclepore. While the basic experiment is one of fluid behavior at a fixed temperature, the presence of *superfluid* liquid ^{4}He allows novel techniques to be used to measure the chemical potential in the system and enhances the temperature homogeneity of the sample. It also results in a rapid response of the pores to changes in the chemical potential.

Third sound is a surface wave excitation on a superfluid helium film,[33] an excitation that can be pulsed. The third-sound time of flight τ is a function of the chemical potential, and therefore measurements of τ provide an *in situ* measure of the chemical potential (described below). This offers advantages over the more standard techniques of measuring the vapor pressure or counting (by dosing known amounts) the number of atoms admitted to the sample cell. In order to use third sound in this way in our work, the temperature range studied is limited to $1.3<T<1.8$ K due to our detection techniques.

The results reported here were obtained in a total of seven separate experiments, using two different cryostat inserts and a number of different nuclepore substrates. The first set of experiments incorporated a cryostat insert and a sample chamber immersed in a pumped helium bath. The bath temperature was regulated with a manostat and the use of electronic feedback with a heater in the ^{4}He bath. The second set of experiments utilized a sample chamber connected to a 1-K pot with a base temperature of about 1.3 K. In the chemical-potential range where we measure hysteresis the dominant thermal link between the 1-K pot and the sample cell is the refluxing of the superfluid film in the sample chamber's fill line. The temperature was regulated with an integrating temperature controller and during stable operation, temperature drifts on the order of 1 mK were typical for the duration of the measurements. Two temperature sensors were mounted on the sample chamber: a carbon resistor used with the electronic feedback, and a Lakeshore calibrated Ge thermometer that provided a separate measure of the temperature.

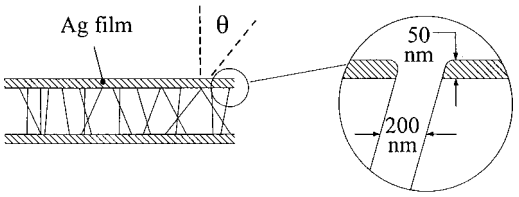

FIG. 7. Cross-sectional diagram of an Ag capacitor on nuclepore (not to scale). The metal film does not block the pore opening, although it may modify the geometry of the opening to some extent.

The sample chamber contained two adsorption substrates. The first substrate was a single nuclepore sheet and the amount of ^{4}He in the pores was detected using a capacitive technique to be described shortly. The second substrate was a borosilicate glass microscope slide on which third-sound pulses were thermally created and measured. In addition, a film reservoir consisting of 200 sheets of 400-nm pore-diameter nuclepore providing 4.9 m^2 of surface area was used in four of the experiments. This reservoir did not influence the measurements of the hysteresis behavior, but it did stabilize the chemical potential. In all of the experiments described, ^{4}He gas was either added or removed at a constant rate, equivalent to changing the adsorbed flat-surface ^{4}He film thickness at a rate of 0.5–2 monolayers/hour. One monolayer of ^{4}He was taken to have a thickness of 0.36 nm. The adsorption results did not depend on the flow rate for these small values, and when the flow was stopped no relaxation effects were observed.

A. Nuclepore capacitor

The amount of ^{4}He in the nuclepore was detected by monitoring changes in capacitance. A parallel-plate capacitor was made by evaporating $\approx$50 nm of Ag on each side of a thin nuclepore sample, see Fig. 7. The Ag film does not block the pore openings at the surface.[14] When ^{4}He liquid enters the pores, the effective dielectric constant (and therefore the capacitance) between the plates changes. The dielectric constant κ of ^{4}He is related to the atomic polarizability[34] by the Claussius-Mossotti equation[35]

$$\alpha = \frac{3V_m}{4\pi}\left(\frac{\kappa-1}{\kappa+2}\right), \tag{9}$$

where $\alpha = 0.1234$ cm^3/mole is the polarizability of ^{4}He and V_m is the molar volume. The capacitance was measured with an Andeen-Hagerling self-balancing capacitance bridge operating at 1000 Hz and the data was recorded by a computer.

B. Chemical potential from the third-sound time of flight

Given the large size of the pores in nuclepore, capillary condensation occurs very close to saturated vapor pressure, requiring a sensitive monitor of the chemical potential. As noted, the velocity of the third sound, a wave on superfluid ^{4}He films in which both the temperature and film thickness

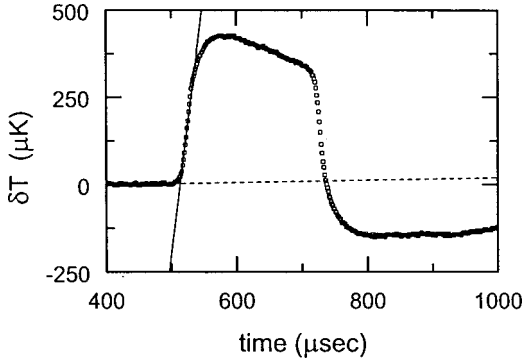

FIG. 8. Temperature signature of a 200-μsec-duration third-sound pulse at $T=1.45$ K. From the intersection of the fitted lines, the arrival time is $\tau=514$ μsec. For this case the film thickness is $d=6.09$ layers and the chemical potential is $\mu=-0.1045$ K.

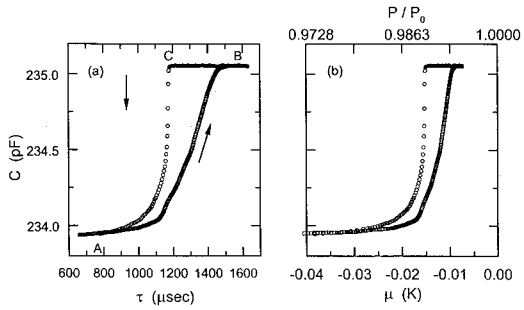

FIG. 9. Global hysteresis loop for 200-nm pore-diameter nuclepore at $T=1.45$ K. In (a), the measured capacitance as a function of the third-sound time of flight τ is displayed. In (b), τ has been used to find the chemical potential (bottom axis) and reduced pressure (top axis).

oscillate, provides such a monitor. We thermally generate a third-sound pulse on the flat glass microscope slide in the sample volume by driving a current pulse of duration W through an Ag strip (18 mm$\times$0.15 mm$\times$50 nm) previously deposited on the glass surface by vacuum evaporation. The wave propagates along the length of the slide and the associated temperature fluctuation is detected with a current-biased Al-thin film thermometer (18 mm$\times$0.15 mm$\times$30 nm). Under typical operating conditions the thermometers have a sensitivity $dR/dT\sim 800$ Ω/K when operated with a dc bias current ~ 70 μA. The detected temperature signal for a $W=200$-μsec wide drive pulse is shown in Fig. 8. The time of flight τ is readily found at the intersection of two lines, one fitted to the baseline before the pulse arrival (dashed line in Fig. 8) and the other fitted to the rising temperature signal (solid line in Fig. 8). For this pulse, $\tau=514$ ± 1 μsec. With the measured time of flight of the pulse τ and the separation of the driver and detector Δx, the velocity is $C_3=\Delta x/\tau$. The square of the superfluid velocity[36,37] is proportional to the superfluid fraction (since only the superfluid moves) of the film and the restoring force due to the van der Waals interaction, and in this temperature range is given by

$$C_3^2=\left\langle\frac{\rho_s}{\rho}\right\rangle\left(1+\frac{TS}{L}\right)^2\frac{k_B\gamma\xi(3\gamma+4\xi)}{m_4 d^3(d+\xi)^2}, \tag{10}$$

where S is the entropy, L the latent heat, k_B Boltzmann's constant, m_4 the mass of ^{4}He, $\gamma=27$ layers^3/K, and $\xi=41.7$ layers.[38] The effective superfluid fraction $\langle\rho_s/\rho\rangle$ is slightly reduced from the bulk superfluid fraction since the binding of ^{4}He is very strong close to the substrate and is empirically given by

$$\left\langle\frac{\rho_s}{\rho}\right\rangle=\frac{\rho_s}{\rho}\left(1-\frac{a+bT(\rho/\rho_s)}{d}\right), \tag{11}$$

where the parameters for glass[39] are $a=0.5$ layers and $b=1.13$ layers/K. Using the measured C_3, Eq. (10) is numerically solved for the film thickness on glass d. Finally, Eq. (3) is used to determine the chemical potential in the sample chamber. For the example pulse in Fig. 8, $d=6.01\pm 0.01$ layers and $\mu=-0.1045\pm 0.0005$ K. The absolute value of the chemical potential is less critical than changes in the chemical potential, and this third-sound technique is able to measure such changes with substantial precision.

IV. RESULTS AND DISCUSSION

Our results are presented in three sections. First, the general features of hysteresis are presented and discussed. Next, we argue that pore intersections are critical to the understanding of the behavior of the hysteresis in nuclepore. Finally, using a model for pore blocking, we calculate pore size distributions and extract information about the number of pore intersections for nuclepore.

A. Features observed in the hysteresis curves

Completely filling and then draining the voids in a porous material maps out the global hysteresis loop. The global loop for nuclepore with 200-nm-diameter pores is shown in Fig. 9(a) for $T=1.45$ K, where squares denote the primary filling (adsorption) curve and circles the primary draining (desorption) curve. While ^{4}He is continuously added or removed, we measure the capacitance C, which provides a measure of the filling fraction for the nuclepore, and we measure the time of flight τ of a third-sound pulse, which provides a measure of the chemical potential. At A, none of the pores have capillary condensed, and a thin film of ^{4}He is present on all of the surface area of the nuclepore. Adding ^{4}He increases the chemical potential and leads to a slowly increasing capacitance and to an increase in τ due to the thickening film. Near $\tau=1100$ μsec, the slope of the primary adsorption curve increases as pores begin to capillary condense. Near $\tau=1500$ μsec, all of the pores have completely filled (point B). Upon removing ^{4}He, pore draining does not occur until the abrupt steep decrease in capacitance begins at point C. This is the region where close observation reveals avalanches in the draining curve.[6,10] We will report on the avalanche behavior separately. With further reduction of μ, all of the pores empty and the hysteresis ends at $\tau\sim 800$ μsec.

In Fig. 9(b), we show the hysteresis loop as a function of μ where we have used the procedure described earlier to

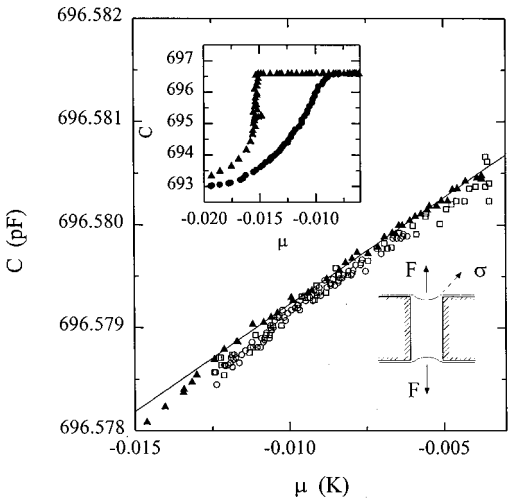

FIG. 10. Linear behavior of the primary draining curve for $\mu > \mu_{corner}$ at $T=1.78$ K. Main figure: closed triangles indicate primary draining, and the solid line is fit to these points. Open symbols indicate that cycling μ down (circles) and then up (squares) is not hysteretic. Insets: view of the global loop and diagram of the origin of the negative pressure felt by the fluid in a filled pore.

determine μ from the measured values of τ. On the top axis, values of P/P_0 [calculated using μ and Eq. (2)] are also shown for reference. If $P/P_0=1$, bulk liquid would be present at the bottom of the sample chamber, and $\mu=0$. The nominally 200-nm-diameter nuclepore pores studied here capillary condense very close to saturated vapor pressure, but the ability of the third-sound technique to precisely track changes in the chemical potential allows measurements quite close to saturated vapor pressure.

In the earlier discussion of capillary condensation of ^{4}He in a 200-nm-diameter cylindrical pore, the filling and draining chemical potentials were calculated to be -0.0135 and -0.0216 K, respectively. From Fig. 9(b), the hysteretic region ranges from approximately -0.008 to -0.030 K. As might be expected, due to the presence of a distribution of pore sizes, this range of chemical potentials spans that of a nominal single ideal cylindrical pore.

B. Negative pressures and compressibility

The most obvious feature in the global hysteresis loop is the sharp corner at the onset of draining on the primary desorption curve. Such a corner in hysteresis data of this type can be suggestive of invasion percolation behavior; as the chemical potential decreases, open volume invades places that were once filled with fluid. Even before any pores drain, however, the capacitance begins to decrease very slightly between points B and C in Fig. 9. When plotted on a very expanded scale as a function of the chemical potential, shown in Fig. 10 at $T=1.78$ K, this initial decrease is linear and it is *not* hysteretic. The upper left inset shows the global hysteresis loop, where the data in the main figure are an expanded view of the horizontal flat-top region of the draining curve well removed from the region of the precipitous drop. The initial decrease in this region is less than 0.1% of the total change in capacitance for complete draining. One possible reason for the slight decrease in capacitance is that there are a very few large pores in the nuclepore that are filling and draining. If so, partial draining and then refilling should be hysteretic. The open symbols show such a partial draining (squares) and refilling (circles). Since no hysteresis is present, this capacitance decrease is not likely to be due to capillary condensation. A second possibility is that the chemical potential was not raised enough for the largest pores to fill. Then, the capacitance changes could be from changes in the film thickness present in the empty pores. We will return to this later. Finally, the capacitance decrease can result from a change in the capillary condensed density (and therefore the effective dielectric constant). A change in density can occur as a result of the finite isothermal compressibility.[5] We discuss this next.

Assuming the third mechanism, the slope of the line in Fig. 10 should provide information about the isothermal compressibility K relating changes in the molar volume δV_m to changes in the pressure δP that the fluid experiences:

$$\frac{\delta V_m}{V_m} = -K\,\delta P. \tag{12}$$

The origin of the pressure is shown in the cross-sectional diagram of a cylindrical pore shown as an inset in Fig. 10. Below saturated vapor pressure, a meniscus forms at the pore opening and a net outward force $F=2\pi R\sigma\cos\theta$ is exerted at each end of the cylinder, where σ is the surface tension and θ is the angle between σ and F. These outward forces put the liquid in the pore under negative pressure $P=-2\sigma/r_m$, where r_m is the meniscus radius of curvature. Using Eq. (7) to relate P to μ, we find

$$P=-\frac{R\mu}{V_m}, \tag{13}$$

where here R is the gas constant. For $KP \ll 1$, integration of Eq. (12) combined with the Claussius-Mossotti equation [Eq. (9)] results in a linearly decreasing capacitance as a function of μ

$$C(\mu)=C(0)+\frac{KR\Delta C}{V_{m0}}\mu, \tag{14}$$

where $C(0)$ and V_{m0} are the capacitance and molar volume at $\mu=0$, and ΔC is the total change in the capacitance from empty to filled pores.

For the data shown in Fig. 10, $C_f=696.581$ pF (extrapolating the line to $\mu=0$) and $\Delta C=3.988$ pF. The fitted line $C=696.581+0.2076\mu$ leads to an isothermal compressibility $K=1.73\times10^{-2}$ bar^{-1}. A summary our compressibility results for measurements of draining for several runs is shown in Fig. 11. These results were collected for a number of different experiments conducted under different conditions and with different nuclepore samples. Measurements of K using data such as these obtained while draining nuclepore without an additional film reservoir in the apparatus (squares) are compared in Fig. 11 to compressibility results by Maynard[40] (diamonds) extracted from second-sound data.

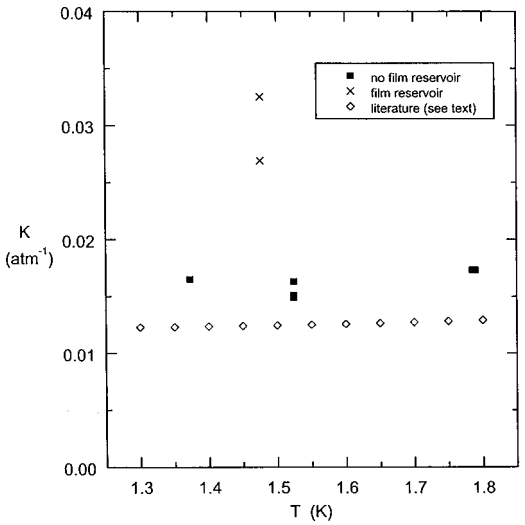

FIG. 11. Compressibility calculated from primary draining curve (solid squares, crosses) compared to previous more-direct measurements by Maynard[40] (open diamonds) to show consistency.

When the sample cell contains 100 sheets of nuclepore with the larger pore diameter of 400 nm, our values for K are shifted to somewhat higher values as shown by the crosses in Fig. 11.

The presence of the film reservoir does not actually change the compressibility, rather, it makes the second mechanism discussed above (film effects) more likely. Since K is calculated from the slope of C vs μ, any additional mechanism that works to increase the slope will lead to a higher apparent compressibility. Without the film reservoir present, it was easy to add enough ^{4}He to completely fill the pores and approach $P=P_0$, although we sometimes did not allow the exact condition $P=P_0$ to be reached. When the additional sheets of 400-nm-nuclepore are present, a small number of the largest pores in 200-nm nuclepore do not fill in our experiments before the chemical potential is reduced. The smallest pores in 400-nm nuclepore are expected on the basis of theory to begin to capillary condense at about half the chemical potential where the smallest pores in 200-nm nuclepore begin to capillary condense, that is, at $\mu_{400} \sim -0.008$ K. When 400-nm nuclepore sheets are present, there is a large volume available as the smallest pores in 400-nm-nuclepore begin to capillary condense. This pins the chemical potential for the low flow rates of ^{4}He that we used. The film thickness in these few large pores changes with chemical potential, leading to an additional decrease in the capacitance and a larger apparent value for K.

C. Subloops

The interior of the global hysteresis loop can be accessed by reversing the flow of ^{4}He when the sample is either partially filled or partially empty in the hysteretic region. In Fig. 12 we show two examples of subloops for 200-nm-diameter nuclepore at $T=1.52$ K, one initiated on the primary filling curve (BCB) and one initiated on the primary draining curve (FGF). First considering BCB, we begin with all of the pores drained (with μ well below point A). Upon adding

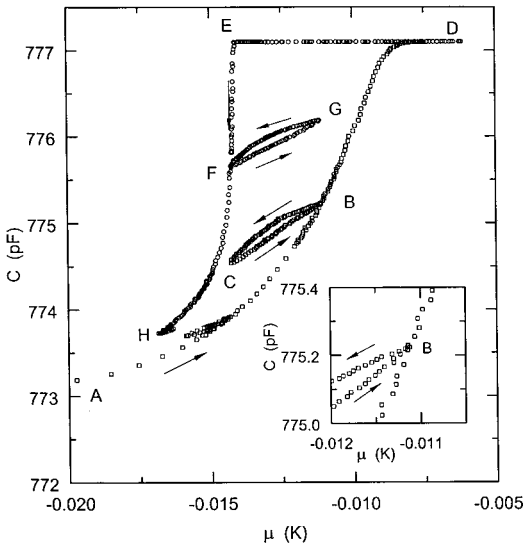

FIG. 12. Subloops for 200-nm pore-diameter nuclepore at $T=1.52$ K. The inset magnifies the connection of BCB to the primary filling curve where we observe return point memory. Return point memory is also observed at point F.

^{4}He, μ increases beyond point A until $\mu_B=-0.0111$ K (point B), and the capacitance follows the primary filling curve to reach point B. At point B, we stop adding ^{4}He gas and begin removing it. Filled pores begin to drain and the ^{4}He film in empty pores thins, and both the capacitance C and μ decrease along the upper trajectory BC. At $\mu_C=-0.0143$ K (point C), ^{4}He is added and the system responds following the lower CB trajectory. As the system returns to point B, the capacitance and μ return to exactly the same value as they had initially (see inset to Fig. 12) demonstrating a property called return point memory (RPM). Further increase in μ results in a sharp change of slope of the filling trajectory in the C-μ plane at point B as the system rejoins the global hysteresis loop and begins to follow the trajectory BD.

If the initial decrease in capacitance along the trajectory BC were only due to film thinning in the empty pores, no subloop would exist, and the return path CB would follow the same trajectory as the initial path BC. Since the subloop is open, the pores have drained and refilled, but have refilled *in a different order*. Using the fractional change in capacitance, the pore density for 200-nm pore-diameter nuclepore, and the area of the capacitor plates, approximately 1.5×10^8 pores have drained and refilled in sweeping out the subloop BCB. It is interesting to note that a significant amount of pore draining has occurred, especially since along the primary draining curve DE in the same chemical-potential range that is spanned by CB, no pore draining has occurred. The second subloop FGF, initiated on the primary draining curve, also exhibits RPM and displays a corresponding kink in the slope as it rejoins the primary desorption curve. In Fig. 13, an example of a more complicated chemical-potential trajectory is shown with two levels of subloops (BEB being the first, CDC and FGF being the second). Following each subloop, the original global hysteresis trajectory is recovered.

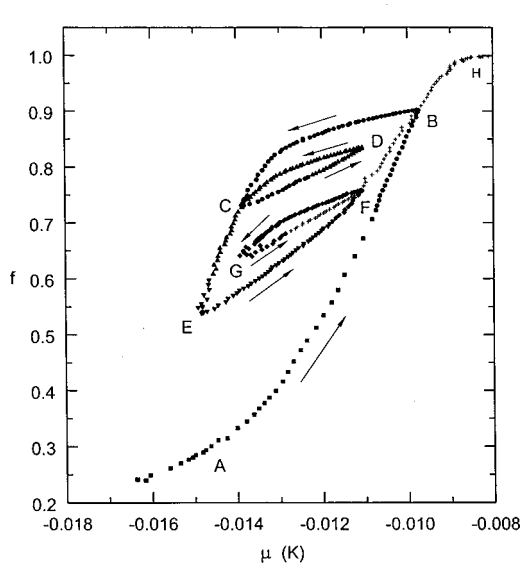

FIG. 13. A set of nested subloops showing multiple occurrences of the return point memory effect at $T=1.524$ K in 200-nm pore-diameter nuclepore.

Using the same diagrams introduced in Fig. 5, both the memory effect and the kink in the slope of the adsorption curve can be understood using the Preisach model. In Fig. 14, the left column shows α-β space with shaded regions indicating which pores are filled. The right column shows the trajectory of the hysteresis curve. The panels show the evolution of a subloop between chemical potential μ_L and μ_R (identifying the right and left endpoints) on the primary adsorption curve using the Preisach model. The top row in Figs. 14(a) and (b) shows that increasing μ sweeps out part of the global loop, i.e., as μ is increased, pores characterized by increasing α values capillary condense. In the second row, reduction of μ uncovers a triangle in α-β space, as a subset of pores drain, i.e., as μ is reduced pores previously filled begin to drain. Those filled pores characterized by the largest β values drain first. The third row shows that exactly the same subset of pores that drained to produce the triangle in α-β space now refills in a different order, leading to an open subloop. Those empty pores characterized by the smallest α values fill first. [The shading in Fig. 14(e) is different for the refilled pores only to emphasize which pores are involved in sweeping out the subloop.] Further, this subloop closes at the same filling fraction and chemical potential (point A), i.e., it returns to the same point demonstrating RPM. Finally, with a continued increase in μ, the kink occurs after the subloop due to the increased phase space of empty pores that is available after the subloop is completed [Fig. 14(g)]. A similar diagram (Fig. 15) and a similar discussion can also be used to demonstrate RPM on the primary desorption branch of the global loop. While the experiment follows the predictions for RPM of the independent pore model here, in the next section we will uncover some important deviations that lead to the rejection of the Preisach model as an appropriate model for capillary condensation in nuclepore. RPM is a robust feature of capillary condensation systems and does not require independent pores.

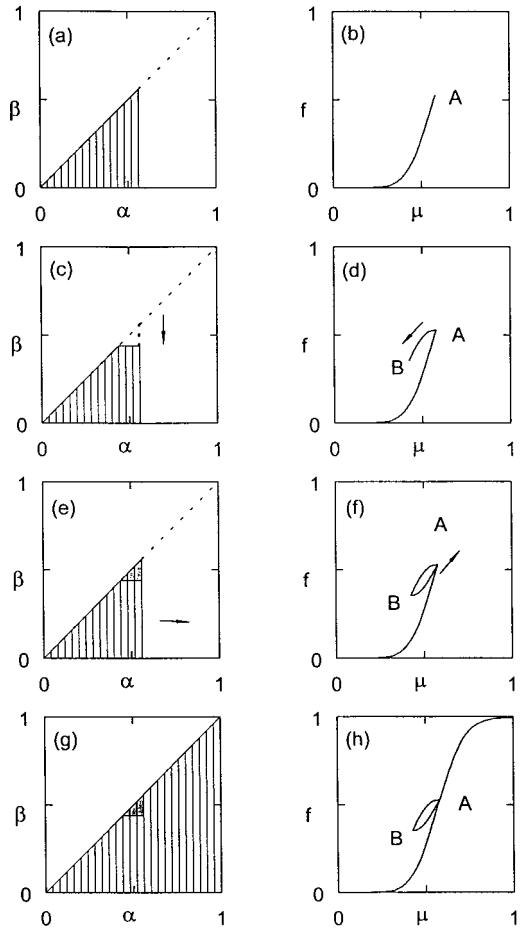

FIG. 14. Example of the development and understanding of return point memory on the primary filling curve using the Preisach model. In α-β space, the small triangle in (c) represents pores that drain when trajectory AB is followed. In all cases the vertical shading lines represent filled pores. The shaded small triangle in (e) represents the filling of those pores when the system follows the trajectory BA. The same pores are refilled, but in a different order, resulting in the open subloop ABA. Upon completion of the subloop ABA, the hysteresis trajectory returns to the primary filling curve at the origin point, point A.

The diagrams in Figs. 14 and 15 suggest another test of the independent pore model. In forming two subloops on the primary filling curve and on the primary draining curve between the *same* chemical-potential endpoints, the *same* subset of pores is involved in each case. It might seem surprising, but this is clear with careful consideration when comparing Figs. 14(e) and 15(e). The only difference between the conditions present during the creation of the different subloops is the number of filled pores in the system in each case that do not drain, and these determine the filling fraction of the left endpoint of the subloop in each case. Therefore, up to a constant offset in filling fraction, the independent pore model predicts that *any* two subloops between *common chemical-potential endpoints* should have exactly the same shape in filling fraction-chemical-potential (i.e., f-μ) space, i.e., they should be congruent. Returning to Fig. 12, the subloops BCB and FGF have common end-

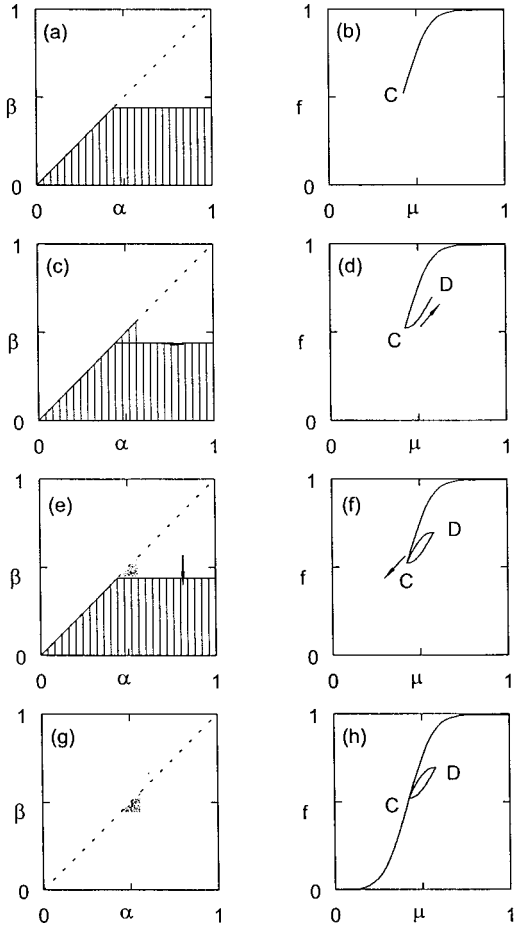

FIG. 15. Example of a subloop on the primary draining curve using the Preisach model. The subloop CDC is created with the *same* triangle of points as ABA in Fig. 14.

points (-0.0143 and -0.0111 K). They appear to be quite similar in shape. To compare the subloop shapes more carefully, the capacitance at the left endpoint C_{left} is subtracted and the results shown in Fig. 16. For BCB, $C_{left}=774.540$ pF and for FGF, $C_{left}=775.657$ pF. The BCB subloop on the adsorption curve (squares) is clearly larger than the FGF subloop on the draining curve (circles). This failure of congruence suggests that additional mechanisms are important

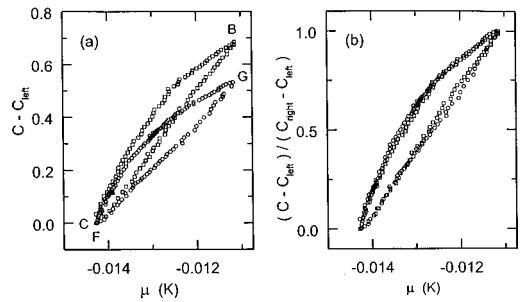

FIG. 16. Comparison of the experimentally measured subloops shown in Fig. 12. In (a), the left endpoint of each subloop is offset to overlap. The loops are not congruent. In (b), the right endpoint is scaled so that both the left and the right endpoints overlap.

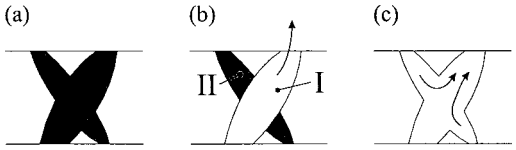

FIG. 17. Diagram of the intersection of two strongly barrel-shaped pores of different diameter to illustrate how pore blocking can occur in nuclepore.

in understanding hysteresis in nuclepore, and that the Preisach model is not entirely adequate.

Thus far internal intersections between the pores in nuclepore have been ignored. Intersections are only important if they allow additional draining pathways to the vapor. For ideal cylindrical pores, intersections play no role. When the larger of two intersecting pores drains, the immediate region of intersection may or may not drain, depending on the detailed nature of the intersection. In the case of perfect intersecting cylinders of different size, if the intersecting region did drain, which is likely, the internal meniscus would retreat into the smaller pore and would have essentially the same radius of curvature as the external opening of the small pore. In nuclepore, the pores are not perfectly cylindrical, but are in fact somewhat barrel shaped, and this might allow pore blocking to become important. To illustrate the general phenomenon that we are considering, consider the diagram of two intersecting strongly barrel-shaped pores in Fig. 17. Initially, the pores can only empty through the surface opening. As ^{4}He is removed, the pore with the largest opening will drain first (pore I here). Once pore I drains, pore II can either drain through the surface ends or through the newly exposed internal openings. In the diagram, the internal opening is larger, and the pore drains immediately. This is an example where blocked access to the vapor limits draining, an effect neglected in the Preisach model. Given the somewhat barrel-shaped pores in the case of nuclepore, this type of pore blocking is likely to be present.

In an effort to qualitatively determine the effect of pore blocking, we now describe a modification to the Preisach model.[8] The feature that this model will account for is the lack of congruence between the subloops shown in Fig. 16(a). The subloop FGF, measured on the draining curve (more inactive pores filled), has a smaller ΔC than BCB measured on the filling curve (less pores filled). That is, subloops between common chemical-potential endpoints at a higher filling factor involve *fewer pores* than those at a lower filling factor. One explanation is that for a higher filling, a fraction of the pores that would normally fill and drain in the subloop do not participate (these pores are *blocked*). To account for the inability of some pores to fill and drain at high filling fractions a modification to the model is made in which a new parameter $0 \leqslant p_i \leqslant 1$ is assigned to each pore, in addition to the filling and draining parameters α_i and β_i. Filling is unaffected by pore blocking, so a pore fills when $\mu > \alpha_i$. Draining, however, requires access to the vapor, so a pore drains when $\mu < \beta_i$ and $\epsilon p_i f < 1$, where ϵ controls the strength of the pore blocking. If $p_i = 0$, no pore blocking

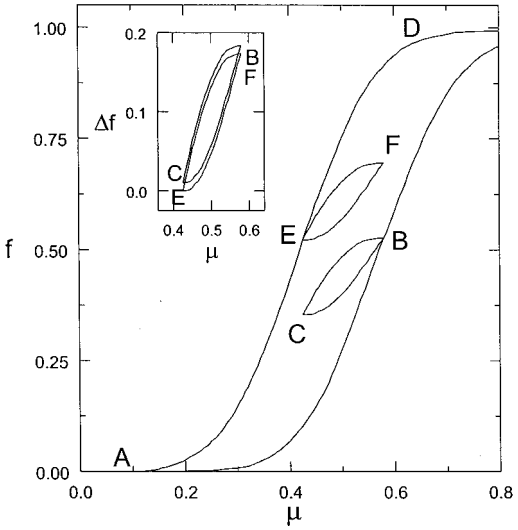

FIG. 18. Calculated subloops using the unmodified Preisach model. The values for α,β are the same as those in Fig. 5(a). Subloops BCB and EFE display RPM and are congruent (see inset, where the subloops have been shifted to bring them in proximity to more clearly show congruence).

occurs. If $p_i \sim 1$, this particular pore won't drain until many other pores in the system drain.

To illustrate the effect of the parameter p, we show the results of two calculations. Figure 18 shows the hysteresis that results for a particular sequence of changes in chemical potential for the case $p=0$ (i.e., Preisach model) for the same choice of α-β pore distribution shown in Fig. 5(a). Figure 19 shows results for numerical simulation using one realization of the modified Preisach model. In the present modified-model calculation (α_i,β_i) are again the same values used in the original demonstration of the Preisach model [Fig. 5(a)] i.e., the pore distribution is the same as in that case. The blocking parameter p_i is assigned a random value between 0.25 and 1.0, and the strength is assigned the value $\epsilon=1.2$. These parameters are selected so that the resulting subloops appear similar to the data and to illustrate the point we are trying to make, but the general conclusions we draw are not affected by the exact choices for the values of the parameters. The filling curve (Fig. 19) is unaffected by p_i, but the draining curve is both steeper and draining is delayed somewhat to lower chemical potentials. Both of these reflect features seen on the primary draining curve in the data, for example in Fig. 9. The two subloops generated within the model, BCB and EFE, are no longer congruent (inset). The subloop at a higher filling fraction (EFE) has a smaller Δf, similar to the data. However, after scaling both the right and left endpoints ($B'C'B'$, offset slightly from BCB for clarity), the *scaled* subloops become congruent. Figure 16(b) shows results from the data of Fig. 16(a) for the 200-nm-nuclepore subloops after scaling both endpoints. Although the scaled subloops have approximately the same shape, they are still not congruent. For the model calculation the area FGF is slightly smaller than $B'C'B'$, similar to the nuclepore data. The qualitative agreement between the modified Preisach model and the data indicate that pore blocking is indeed very important in the nuclepore system.

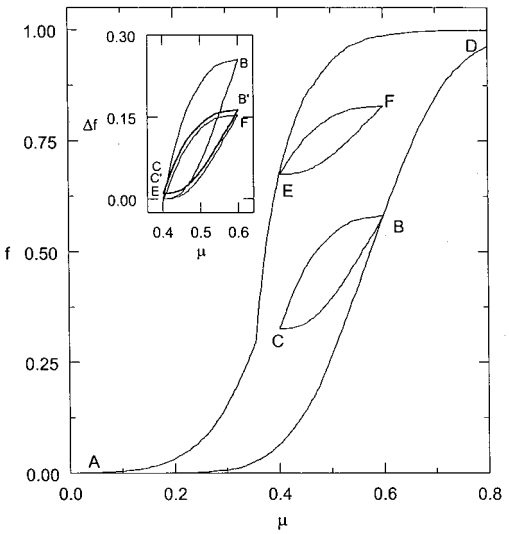

FIG. 19. Calculated subloops using the modified Preisach model. The values for α,β are the same as those in Fig. 5(a). The pore blocking parameters p_i are randomly assigned between 0.25 and 1, and $\epsilon=1.2$. Subloops BCB and EFE display RPM but are not congruent (see inset). If both endpoints are scaled, as shown in $B'C'B'$, the loops become congruent.

In an effort to test a system where pore intersections are less important, we used the guidance from our nuclepore simulation indicating that 30-nm nuclepore is much closer to the percolation threshold, and we did an experimental study of 30-nm pore-diameter nuclepore. Figure 20(a) shows the data for a sequence of subloops (symbols) and a portion of the global loop (solid lines) for the 30-nm pore-diameter nuclepore. The 30-nm-nuclepore global hysteresis loop occupies a chemical potential range from ~ -1 to -0.02 K due to the smaller pore size. The six subloops in Fig. 20 were obtained by creating subloops within subloops (to show all of the trajectories would have made the figure too complicated) so as to create a set of subloops that spanned a common chemical-potential range, but for rather different values of the filling fraction. These subloops are clearly not congruent, from which we conclude that pore blocking remains an important effect. The scaled subloops are almost the same shape, but as for the 200-nm subloops, the ones at the highest filling fraction have smaller areas.

A drawback to using this modified Preisach model is the qualitative and rather arbitrary nature of the parameters. In nuclepore, we have pores with a distribution of sizes that are internally connected. We would like to utilize a model of the hysteresis to extract numbers like the pore size distribution or the number of intersections/pore. Our definitions of p_i and ϵ were motivated by the experimental observation of the failure of congruence (Fig. 16), and our modification of the Preisach model and the resulting consistency with the data enhanced our understanding of the behavior of the hysteresis, and convinces us that pore blocking is a relevant issue in the case of nuclepore, but p_i and ϵ do not represent true physical parameters of the system. In the next section, we use a hys-

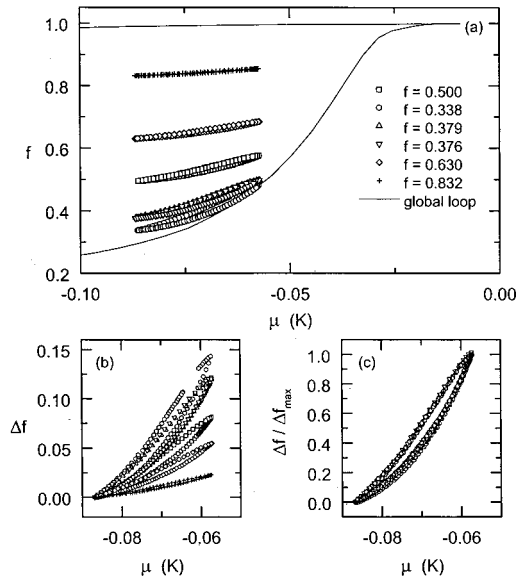

FIG. 20. Subloops measured between the same chemical-potential endpoints for 30-nm nuclepore at $T=1.48$ K. In (a), the six loops are shown with respect to the position of the global loop and in most cases were measured from within larger subloops. In (b), the left endpoint of each loop is offset, with $\Delta f=f-f_{left}$. The larger f_{left}, the smaller the subloop. In (c), the loops are scaled so that both endpoints overlap, where $\Delta f_{max}=f_{right}-f_{left}$. The scaled loops are almost congruent.

teresis model that goes further in allowing one to find the pore size distributions and the connectivity when pore blocking is present.

D. Pore size distributions

With the importance of pore blocking and internal pore connections in nuclepore established, calculations of the pore size distribution can be attempted using the capillary condensation hysteresis model described by Mason. In the Mason model, each pore is described as a cavity with connections (windows) to other cavities. The structure of the cavity network used within the model is a Bethe lattice. In a Bethe lattice, each pore is connected to $\mathcal{C}$ other pores (one parent and $\mathcal{C}$-1 child pores), shown in Fig. 21 (for $\mathcal{C}=4$). The child pores do not connect to each other or to other pores above the parent or to other pores in different lines.[41] The advantage to this particular pore network is that no looping pathways (pathways that start and end on the same pore) occur. Clearly this is not true in most porous materials, but this structure allows analytic results to be found while maintaining the interconnectedness of a real porous material. The internal volume is assumed to be dominated by the cavities, not the windows. Each cavity is characterized by a single size, the radius of curvature r_K, although a distribution of cavity sizes are available. Each window is characterized by a size that must be smaller than the size of the cavity, and a distribution of windows sizes is also available. When capillary condensation is considered for such a system, the pores fill independently, but in order to drain they must meet a condition: at least one of the neighboring pores must be empty for draining to be allowed.

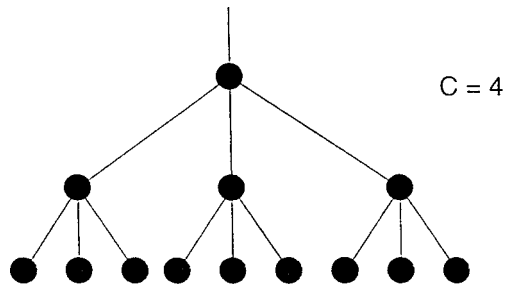

FIG. 21. Drawing of a Bethe tree geometry used by Mason. Disks represent pores and the lines represent internal connections. In this case each pore has four internal connections or windows.

With this basic structure, the model can be used to generate hysteresis curves that depend on the distributions of cavity and window sizes. In particular, a great deal of information is contained in a set of hysteresis curves called secondary desorption curves. Here, beginning with all of the pores empty, they are partially filled to a filling fraction f_{rev}, and then completely drained. A set of such curves is collected by varying f_{rev}. These curves have inherent features very similar to experimentally measured secondary desorption curves. A number of features can be identified (such as the chemical potential at the onset of draining, and a ''knee'' where the slope of draining increases in both the theory and experimental curves). Since the Bethe lattice allows analytic calculations, comparison between the experimental and theory features in the hysteresis curves allows one to estimate cavity sizes, window sizes, and the number of pore interconnections.

For this analysis, the equations governing filling and draining are determined. For convenience, Mason makes a number of definitions. The cavities are characterized by the normalized cavity distribution function $g(r)$, where $g(r)dr$ is the probability of a cavity with a radius between r and $r+dr$. The windows are described by a similar size distribution function $f(r)$. Then, instead of using chemical potentials in the model, two new variables based on the size distribution functions are introduced

$$p=\int_0^{r_K} f(r)dr, \tag{15}$$

$$q=\int_0^{r_K} g(r)dr, \tag{16}$$

where in each case r_K is the Kelvin radius and is related to the chemical potential by the Kelvin equation [Eq. (7)]. The variable p represents the fraction of windows with $r<r_K$, and q represents the probability that a cavity is filled at r_K. For the general case for windows, these variables are related by $p^{\mathcal{C}}>q$, but for the constraint that the largest window size is the size of the cavity, this becomes

$$p^{\mathcal{C}}=q, \tag{17}$$

where $\mathcal{C}$ is the parameter characterizing the number of intersections per pore. With equality, there is an exact relation-

ship between p and q, a constraint we will adopt for the analysis we will carry out. The equality holds when the largest window is the same size as the pore size r_p. Considered independently, this single pore would *not* be hysteretic. However, when a network of such pores is constructed, pore blocking leads to hysteresis. While this constraint will certianly not hold for a general pore space, Mason showed that it is approximately true for a random packing of equal spheres.[42] The value of this approximation is that with it, the connectivity between pores can be determined. The variable S is the number fraction of cavities filled, and V is the experimentally measured value of the net adsorption.

The equations governing primary adsorption and desorption curves are found using the probability arguments. On filling, pore blocking does not play a role, and there is no access condition. The number of pores filled follows from the definition of q,

$$S_a = q, \tag{18}$$

where S_a is the number fraction of the pores filled on the primary adsorption curve. For draining, pore blocking is important, and a pore must first have access to the vapor before it can drain (a neighboring pore must be empty). v is the probability that a window into a pore is connected to the vapor. The equations for the primary draining curve are

$$S_d = (1-v)^{\mathcal{C}/(\mathcal{C}-1)}, \tag{19}$$

$$p = \frac{S_d^{1/\mathcal{C}} - S_d^{(\mathcal{C}-1)/\mathcal{C}}}{1 - S_d^{(\mathcal{C}-1)/\mathcal{C}}}. \tag{20}$$

One of the features to be extracted from the theoretically generated curves and compared to experimental data is the position on the primary desorption curve where the draining commences:

$$p_{corner} = (\mathcal{C}-2)/(\mathcal{C}-1). \tag{21}$$

In capillary condensation, the number fraction of filled pores is not enough information to predict hysteresis curves. This is because ''empty'' pores are not really empty, rather there is a film adsorbed to the surfaces. In order to account for surface adsorption and make direct comparison between experiment and theory, Mason uses a normalized variable for both. For a given number filling fraction F, there is an associated measure $V_F = NF\psi + N(1-F)\chi$, where N is the total number of pores, ψ is the average amount of liquid in the capillary filled pores, and χ is the average amount of surface adsorption in the empty pores. Here ψ and χ are assumed to be independent of cavity size. The normalized variable f_F is the fraction

$$f_F = \frac{V_{max} - V_F}{V_{max} - V_a} = \frac{N(1-F)(\psi-\chi)}{N(1-S_a)(\psi-\chi)} = \frac{1-F}{1-S_a}, \tag{22}$$

where V_{max} is the maximum amount adsorbed when all of the pores are full. The surface adsorption is canceled. We now have a normalized variable that can relate the number fraction filled directly to the experimental measure of adsorption.

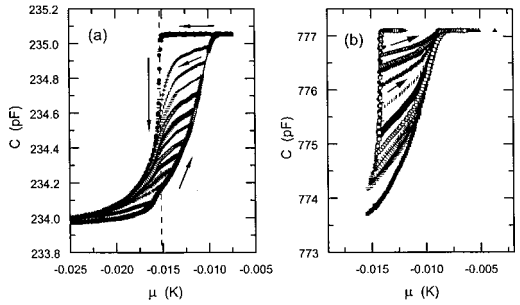

FIG. 22. Reversal curves for nominal 200-nm pore-diameter nuclepore. In (a), secondary draining data is shown at $T=1.52$ K. In (b), secondary filling data is shown at $T=1.45$ K. These data are from two separate experiments that utilized capacitors of different surface area. This explains the different capacitance values. Subfigure (a) is used in the data analysis; subfigure (b) is not used in the analysis and is included for completeness to illustrate the case.

Using the above relations, values of f_F as a function of q (related to μ) can be calculated for the secondary desorption curves. Details of the derivation can be found in Mason's paper.[5] For the turning point q_i, the two equations are

$$p = \frac{q_i^{1/\mathcal{C}}[(1-u)^{1/(\mathcal{C}-1)} - q_i(1-u)]}{1 - q_i(1-u)}, \tag{23}$$

$$f_F = \frac{1 - q_i(1-u)^{\mathcal{C}/(\mathcal{C}-1)}}{1-p^{\mathcal{C}}}, \tag{24}$$

where u is the probability that an initially filled window to a cavity empties at p. Giving q, q_i, and $\mathcal{C}$, and the relation between p and q [Eq. (17)], Eq. (23) can be solved (numerically) for u and all of these relations can be used in Eq. (22) to find f_F.

The experimental data required are a thorough set of secondary draining curves.[43] The secondary filling curve is found by partial draining followed by complete filling; the secondary draining curve is found by partial filling followed by complete draining. The measurements for 200-nm nuclepore used in this analysis are displayed in Fig. 22. Figure 22(a) contains the secondary draining curves at $T=1.52$ K and Fig. 22(b) contains secondary filling curves at $T=1.45$ K. Arrows indicate the direction of changes in μ for the various subsections of the curves. Since pore blocking only affects the draining behavior, there is not much information in the primary filling curves [Fig. 22(b)], but we show them for completeness. The following analysis will use the primary desorption curves in [Fig. 22(a)]. The first step in the analysis is to convert the raw capacitance measurements to the normalized filling fraction variable. In Eq. (22), C_{max}, the maximum capacitance, and C_a, the capacitance of the primary filling curve for a given value of μ, must be determined. Extrapolating the filled region of the hysteresis to $\mu = 0$ results in $C_{max} = 235.0573$ pF. A value $C_a(\mu)$ was interpolated for any value of μ needed. The normalized results

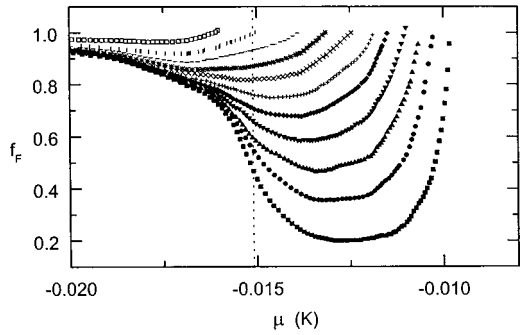

FIG. 23. Secondary desorption data converted into the normalized variable f_F. The dotted line marks the position of the corner where draining begins sharply.

for the Mason variable f_F for 200-nm nuclepore at $T=1.453$ K are shown in Fig. 23. The dashed line marks the onset of draining $\mu_{corner}=-0.0151$ K [this is also shown as a dashed line in Fig. 22(a)]. Notice that two distinct values of f_F for each curve can easily be found: the minimum ($f_{F,min}$) and the value where f_F intersects the dashed line ($f_{F,corner}$). These values may be calculated theoretically in the model, and the calculations compared to the data. It is from that comparison that information about the pore size distribution is determined.

First, given q_i, the beginning of the secondary desorption curve in the model, and $\mathcal{C}$, we can use Eqs. (23) and (24) to calculate one curve of f_F vs q, where q is the integrated cavity size distribution (what we are seeking). This curve will look very similar to one of the curves in Fig. 23, with a clearly defined minimum. From this one curve, we pick off the theoretical value $f_{F,min}$ for the given q_i. Repeating this for 80 different q_i, $0.2<q_i<1$, allows a single curve with 80 $f_{F,min}$ vs q_i values to be plotted. Three such curves are shown as solid lines in Fig. 24(a) for $\mathcal{C}=2.5$, 5, and 10. The three theoretical curves are close together, and unfortunately are *very* insensitive to the choice for $\mathcal{C}$. For reasons to be clarified shortly, we will assume (and show later) that the experimental values of $f_{F,min}$ should reasonably fall on the theoretical curve for $\mathcal{C}=10$. For each value of μ_i we can then associate the corresponding value of q_i from the theoretical line. Since μ_i is related to the pore size via the Kelvin equation, and μ_i is related to q_i by the procedure discussed above, we now have extracted information about the cavity sizes. Before reporting this cavity size information, we will first show why we associated the experimental data with the $\mathcal{C}=10$ curve.

In addition to finding theoretical values for $f_{F,min}$, using the same equations [Eqs. (23) and (24)], we can also calculate $f_{F,corner}$ for each value q_i. For a range of q_i values, we can make a plot of $f_{F,corner}$ vs $f_{F,min}$ to produce the curves shown in Fig. 24(b). Here we show theoretical lines for $\mathcal{C}=2.5$, 5, and 10 along with the values from the experimental data. Comparing the data to the theory, we see that the data best fit the theoretical line for $\mathcal{C}=10$. Unfortunately, the trend of the theoretical lines to get closer together makes it difficult to determine the exact value of $\mathcal{C}$ when $\mathcal{C}$ is large. We also notice that at either end ($f_{F,min}\sim 0.2$ and $f_{F,min}$ ~ 0.9) the data deviate from the theoretical curve. From these three curves, the most reasonable conclusion is that the model predicts more than 5 intersections/pore. Our previous calculations in Sec. II A indicated a lower limit on the average connectivity of 5.3 intersections/pore. This model is consistent with more than 5 intersections/pore.

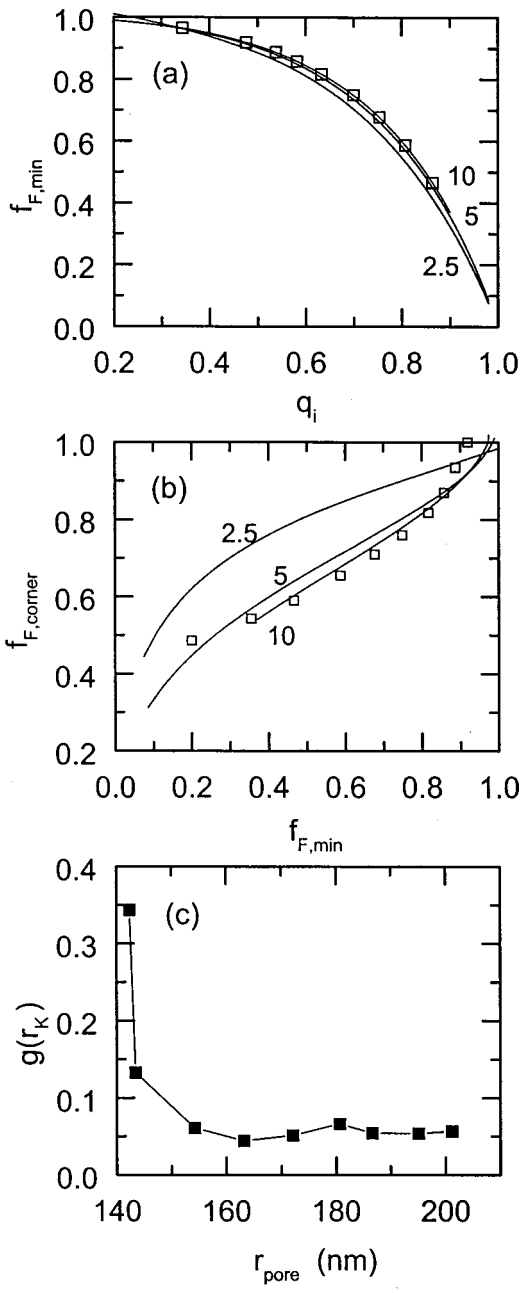

FIG. 24. (a) Determination of the integrated cavity size distribution, (b) pore connectivity, and (c) the normalized cavity size distribution function using the Mason analysis. The solid lines in (a) and (b) are theory calculations for $\mathcal{C}=2.5$, 5, and 10.

We now return to the values for q determined in Fig. 24(a). Using the Kelvin equation, $r_K=-2\sigma V_m/\mu$, we calculate r_K for each value μ_i where a secondary desorption curve began. In Fig. 24(c) the cavity size distribution $g(r)$ is plotted. The Kelvin radius is the mean radius $2/r_K=1/r_1$

$+1/r_2$. Even for our barrel-shaped pores, $r_2 \gg r_1$ since the thickness of the material is ~ 50 times the pore size. We calculate the pore size in Fig. 24(b) as $r_{pore} = r_K/2$. The size distribution function is sharply peaked at $r_{pore} = 140$ nm, with no pores smaller than 140 nm. The probability of larger pores quickly decreases, and in the range 155 nm $< r_{pore} < 200$ nm the probability for finding a pore of any of these sizes is about equal. Ideally, within the Mason model the window size distribution can also be determined. Unfortunately, the large and inaccurate determination of $\mathcal{C}$ prevented the calculation of $f(r)$.

As in previous measurements that utilized the nominal 200-nm diameter-pore nuclepore system,[14,17] the pore sizes were found to be clustered in a narrow spectrum of radii centered at $r_{pore} = 140$ nm with a small and flat tail of larger pores up to $\sim r_{pore} = 200$ nm. In addition, we can estimate about 10 interconnections for each pore. Previous B.E.T. adsorption calculations of pore sizes by Godshalk and Hallock[17] found $r_{pore} \sim 155$ nm for the first layer and ~ 220 nm for the second layer of ^{4}He film. Their calculations based on the hysteresis curves found a peak at $r_{pore} = 130$ nm. While the model used here (a single parameter for filling and draining with pore blocking causing the hysteresis) is much different than the independent pore assumptions made in earlier calculations, the results for the calculated pore sizes are surprisingly similar.

V. CONCLUSIONS

We have presented hysteresis results for ^{4}He liquid in nuclepore. Using the third-sound velocity as an *in situ* monitor of the chemical potential and capacitance techniques to determine the filling fraction, detailed studies of 200-nm-diameter pores that capillary condense close to saturated vapor pressure are possible. Qualitative observation of properties of the hysteresis curves reveals information about the adsorbate and the porous material. When all of the pores were filled, a slight decrease in the density of ^{4}He liquid as the chemical potential was reduced is shown to be due to the isothermal compressibility of the liquid. Hysteresis subloops demonstrate the property of return point memory, but subloops between the same chemical-potential endpoints are not congruent. This indicates that the Preisach model, a model for independent pore elements, is not adequate for understanding the hysteresis observed. Modifying the Preisach model to account for the inherent connectivity in nuclepore shows qualitatively that pore blocking is present. Finally, using a model for capillary condensation that relies only on pore blocking, we have some success in the determination of pore size distributions and pore connectivity information for 200-nm pore-diameter nuclepore. More broadly, this work demonstrates the suitability of a novel working fluid, superfluid ^{4}He, for such measurements. Given the rapid equilibration times for superfluid ^{4}He, the approach may be of general value in the study of other porous materials.

ACKNOWLEDGMENTS

We acknowledge helpful discussions with R.A. Guyer and J.A. Krumhansl. This work was supported by the National Science Foundation through Grant Nos. DMR 94-22208, DMR 97-29805, and DMR 98-19122 and by research trust funds provided by the University of Massachusetts at Amherst.

*Present address: Sandia National Laboratories, Albuquerque, NM.
†Email address: hallock@physics.umass.edu

[1] D. H. Everett, in *The Solid-Gas Interface*, edited by E. A. Flood (Marcel Dekker, New York, 1967), Vol. 2, Chap. 36, p. 1055.
[2] F. Preisach, Z. Phys. **94**, 277 (1935).
[3] M. Sahimi, Rev. Mod. Phys. **65**, 1393 (1993).
[4] G. Mason, Proc. R. Soc. London, Ser. A **390**, 47 (1983).
[5] G. Mason, Proc. R. Soc. London, Ser. A **415**, 453 (1988).
[6] M. P. Lilly, P. T. Finley, and R. B. Hallock, Phys. Rev. Lett. **71**, 4186 (1993).
[7] M. P. Lilly and R. B. Hallock, Czech. J. Phys. **46**, 141 (1996).
[8] M. P. Lilly and R. B. Hallock, in *Dynamics in Small Confining Systems II*, edited by J. M. Drake, S. M. Troian, J. Klafter, and R. Kopelman, MRS Symposia Proceedings No. 366 (Materials Research Society, Pittsburgh, 1995), p. 241.
[9] M. Lilly and R. Hallock, J. Low Temp. Phys. **101**, 385 (1995).
[10] M. P. Lilly, A. H. Wootters, and R. B. Hallock, Phys. Rev. Lett. **77**, 4222 (1996).
[11] Nuclepore is a product of Costar, Cambridge, MA.
[12] We define the *primary hysteresis loop* to be the locus of data representing the fraction of the porous material that is filled as a function of a continuous evolution of the chemical potential from low values to values that approach saturated vapor pressure and then back to the original very low values. We define the branch of the hysteresis curve that develops as the chemical potential increases in such a continuous evolution to be the *primary filling curve* or the *primary adsorption curve*. Similarly, we define the branch of the hysteresis curve that develops as the chemical potential decreases from values near saturated pressure to be the *primary draining curve* or the *primary desorption curve*. We will use such terms interchangeably but be more precise about adsorption (e.g., growth of a film on a surface), and draining (e.g., the loss of liquid from pore spaces) in cases where there might be some ambiguity.
[13] D. S. Cannell and F. Rondelez, Macromolecules **13**, 1599 (1980).
[14] D. T. Smith, K. M. Godshalk, and R. B. Hallock, Phys. Rev. B **36**, 202 (1987).
[15] The nuclepore samples we have studied here are characterized by [nominal pore diameter (R), number of pores/cm^2 (n), and polycarbonate film thickness (t)] values of [30 nm, 6×10^8 pores/cm^2, 6 μm] and [200 nm, 3×10^8 pores/cm^2, 10 μm].
[16] J. M. Valles, Jr., D. T. Smith, and R. B. Hallock, Phys. Rev. Lett. **54**, 1528 (1985).
[17] K. M. Godshalk and R. B. Hallock, Phys. Rev. B **36**, 8294 (1987).
[18] R.A. Guyer and K.R. McCall (unpublished); R. A. Guyer (private communication).
[19] Liquid ^{4}He wets almost all materials including nuclepore. The only known cases of nonwetting behavior of ^{4}He are some of the alkali metals.

[20] J. Israelachvili, *Intermolecular & Surface Forces* (Academic Press, New York, 1992).
[21] We have deviated from the usual convention of using α and β for the van der Waals parameters and substitute γ and ξ, respectively, to reserve α and β to denote pore filling and emptying parameters.
[22] H. B. G. Casimir and D. Polder, Phys. Rev. **73**, 360 (1948).
[23] E. S. Sabisky and C. H. Anderson, Phys. Rev. A **7**, 790 (1973).
[24] M. W. Cole and W. F. Saam, Phys. Rev. Lett. **32**, 985 (1974).
[25] W. F. Saam and M. W. Cole, Phys. Rev. B **11**, 1086 (1975).
[26] J. Ortin, J. Appl. Phys. **71**, 1454 (1992).
[27] R. A. Guyer, K. R. McCall, and G. N. Boitnoff, Phys. Rev. Lett. **74**, 3491 (1995).
[28] D. H. Everett, J. Colloid Interface Sci. **52**, 189 (1975).
[29] I. D. Mayergoyz, J. Appl. Phys. **57**, 3803 (1985).
[30] T. Doong and I. D. Mayergoyz, IEEE Trans. **21**, 1853 (1985).
[31] K. R. McCall and R. A. Guyer, J. Geophys. Res., [Space Phys.] **99**, 23 887 (1994).
[32] G. C. Wall and R. J. C. Brown, J. Colloid Interface Sci. **82**, 141 (1981).
[33] K. R. Atkins and I. Rudnick, *Progress in Low Temperature Physics*, edited by C. J. Gorter (North-Holland, Amsterdam, 1970), Vol. VI; K. S. Ketola, S. Wang, P. Lemaire, and R. B. Hallock, J. Low Temp. Phys. **119**, 645 (2000).
[34] J. D. Jackson, *Classical Electrodynamics* (Wiley, New York, 1975).
[35] Here we use the traditional α to denote the atomic polarizability as it does not introduce confusion.
[36] D. Bergman, Phys. Rev. **188**, 370 (1969).
[37] D. J. Bergman, Phys. Rev. A **3**, 2058 (1971).
[38] S. J. Putterman, *Superfluid Hydrodynamics* (North-Holland, Amsterdam, 1974).
[39] J. H. Sholtz, E. O. McLean, and I. Rudnick, Phys. Rev. Lett. **32**, 147 (1974).
[40] J. Maynard, Phys. Rev. B **14**, 3868 (1976).
[41] This lattice is obviously not correct for nuclepore, where interconnections within the material can form loops. That is, following pore intersections might lead back to the initial pore. However, this lattice is only chosen as a tractable example to address pore blocking.
[42] G. Mason, J. Colloid Interface Sci. **35**, 279 (1971).
[43] A complete set of secondary adsorption and desorption data was not available for 30-nm-diameter nuclepore, so the PSD analysis is only presented for 200-nm nuclepore.